Journal of Computational Physics **153,** 638–659 (1999)
Article ID jcph.1999.6298, available online at http://www.idealibrary.com on IDEAL®

Comparing Two Topography-Following Primitive Equation Models for Lake Circulation

L. Umlauf,* Y. Wang,† and K. Hutter‡

Department of Mechanics, Technical University of Darmstadt, Hochschulstrasse 1, 64289 Darmstadt, Germany
E-mail: *umlauf@mechanik.tu-darmstadt.de, †wang@mechanik.tu-darmstadt.de,
and ‡hutter@mechanik.tu-darmstadt.de

Received July 6, 1998; revised May 5, 1999

We compare two semi-implicit models with topography-following coordinates for the solution of the shallow water equations. The models are identical in horizontal representation, but model A applies a vertical finite difference method and model B a vertical spectral method. Convergence, stability, and performance for different geometries and parameters are compared. We report our experiences gained in lake modelling with these models and give some results of simulations of Lake Ammer in the homogeneous and stratified cases. Different wave phenomena and the basin wide circulations will be discussed.

Key Words: benchmark; stability; shallow water; semi-implicit; lake; circulation; limnology; spectral.

1. INTRODUCTION

Recently there have been many approaches to replacing spatially one-dimensional hydrodynamical models by three-dimensional models as a management tool for the prediction of water quality in lakes and reservoirs. Due to the fast advance in computational fluid dynamics there is a wide range of such models between finite difference methods (FD), spectral methods (SP), finite element methods (FEM), and finite volume methods (FVM) and combinations thereof [12, 22, 4, 19, 23]. FD models, about which we are concerned in this paper, are generally distinguished by those using Cartesian coordinates and those using topography-following coordinates. Many models stem from oceanography but there are others, using professional FEM packages, suited to solving the shallow water equations.

A precise prediction of water quality is always based on a reliable turbulence closure and requires stability of the hydrodynamical model over a large range of horizontal and, in

0021-9991/99 $30.00

particular, vertical turbulent diffusivities. The most severe time step limitation arises from the stability criterion associated with the vertical diffusion terms and may be overcome by the formulation of (semi-)implicit temporal integration procedures. However, there are still other effects discussed in this paper that are related to the smaller length scales of a lake compared to the scales of the ocean that make it a difficult task to economically integrate the shallow water equations in a lake over several months.

In this paper we shall compare two such models and test their applicability to the calculation of the wind forced response of a lake or a reservoir. Both are based on SPEM by Haidvogel *et al*. [12] and Hedstrom [13] but have been slightly modified to suit the special conditions envisaged by us.

Model A is a semi-implicit generalized σ-coordinate model and employs a vertical finite difference technique (see Song and Haidvogel [22]). It has been modified by Güting [10], and a k-ϵ-closure has been added. However, the specialties of turbulence closure wil not be discussed here.

Model B is the original semi-spectral σ-coordinate model (SPEM) that has been modified by Wang and Hutter [26] to allow for a semi-implicit (vertical) time stepping of either Crank–Nicolson or backward Euler type. In the horizontal direction both models employ an identical centered FD discretization on a staggered Arakawa grid in connection with a conformal mapping of the irregular shoreline to a rectangle to achieve higher smoothness of the horizontal boundary conditions.

The paper is structured as follows: In Section 2 we give a short introduction to both models and to the boundary- and topography-following coordinate system. In Section 3 we continue with the comparison of the different time-stepping schemes and the numerical representation of the vertical direction. Section 4 then discusses the numerical particularities in lake modelling compared to those of ocean modelling and some complications arising from the topography-following σ-coordinate system. In Section 5 we compare the stability, accuracy, and performance of models A and B for a rectangular basin and for Lake Ammer, a medium size Alpine lake in southern Germany. The simulation results for Lake Ammer in the homogeneous and in the density stiatified case will be discussed in Section 6. We will show that both models are able to reproduce inertial, Kelvin, and Poincaré-type waves. We conclude with a summary and some remarks in Section 7.

2. MODEL FORMULATION

2.1. *The Topography-Following Coordinate System*

The equations of motion for a lake or a reservoir can be derived in a standard way from the Navier–Stokes equations in a rotating system. Invoking the Boussinesq and the Shallow-Water Assumptions leads, after an appropriate scaling, to the classical hydrostatic primitive equations (PE) (see, e.g., Hutter [16]).

Common numerical techniques for the solution of the PE employ a Cartesian coordinate system where the vertical grid size can be easily arranged to allow higher resolution in regions of strong gradients in the surface layer of a lake (epilimnion) and near the thermocline (metalimnion).

Since varying topography and sediment exchange processes play a crucial role in lake modelling we use a model with generalized vertical σ-coordinates ("s-coordinates") that

follow the bathymetry and greatly simplify the computation and formulation of the flux boundary conditions. This coordinate system, introduced first by Song and Haidvogel [22], consists of the terms

$$z = h_c s + (h - h_c)C(s), \qquad H_\theta \equiv \frac{\partial z}{\partial s}, \qquad -1 \le s \le 0, \tag{1}$$

$$C(s) = (1-b)\frac{\sinh(\theta s)}{\sinh\theta} + b\frac{\tanh[\theta(s+1/2)] - \tanh((1/2)\theta)}{2\tanh((1/2)\theta)}, \tag{2}$$

where θ and b are the surface and bottom control parameters; h_c is a constant chosen to be the minimum depth or a width of the surface or bottom boundary layer in which a higher resolution is required. The traditional σ-coordinates, first introduced by Phillips [20] (where s is proportional to z), can be recovered by letting the parameter θ approach zero. There are three attractive features of the s-coordinate transformation in lake modelling:

1. A high vertical resolution can be achieved in the epi- and metalimnion by appropriately choosing the parameter θ even for uniform grid spacing in the computational domain. This makes it possible to efficiently simulate turbulent mixing processes in the surface layer.
2. A coarse resolution in the less active bulk (hypolimnion) saves computation time.
3. A higher resolution in the bottom boundary layer can be obtained by an appropriate choice of the parameter b, e.g., to resolve processes in the turbulent boundary layer.

2.2. *The Horizontal Curvilinear Coordinates*

To sidestep the approximation of an irregular lateral lake boundary by a horizontal Cartesian grid and to avoid the interpolation of lateral boundary conditions to the numerical boundary both models make use of a horizontal conformal mapping. The resulting curvilinear boundary-following coordinate system is able to provide a spatially variable horizontal grid resolution. We used a software package developed by Wilkin and Hedstrom [27] for the generation of the two-dimensional orthogonal grid. For lakes that have suitably smooth boundaries this package provides the metric coefficients m and n of the conformal mapping from an irregular lake shoreline to a rectangle.

Let the new coordinates be $\xi(x, y)$ and $\eta(x, y)$; then the relationship of horizontal are lengths in the mapped and the physical domains is given by

$$(ds)_\xi = \left(\frac{1}{m}\right)d\xi, \tag{3}$$

$$(ds)_\eta = \left(\frac{1}{n}\right)d\eta. \tag{4}$$

After the conformal mapping the PE in s-coordinates can be written, as shown by Arakawa and Lamb [1] and Kasahara [17], as

Balance of mass:

$$\frac{\partial}{\partial\xi}\left(\frac{H_\theta}{n}u\right) + \frac{\partial}{\partial\eta}\left(\frac{H_\theta}{m}v\right) + \frac{\partial}{\partial s}\left(\frac{H_\theta}{mn}\Omega\right) = 0. \tag{5}$$

Balance of momentum:

$$\frac{\partial}{\partial t}\left(\frac{H_\theta}{mn}u\right)+\frac{\partial}{\partial \xi}\left(\frac{H_\theta}{n}u^2\right)+\frac{\partial}{\partial \eta}\left(\frac{H_\theta}{m}vu\right)+\frac{\partial}{\partial s}\left(\frac{H_\theta}{mn}\Omega u\right)$$
$$-\left\{v\frac{\partial}{\partial \xi}\left(\frac{1}{n}\right)-u\frac{\partial}{\partial \eta}\left(\frac{1}{m}\right)\right\}H_\theta v-\frac{H_\theta}{mn}fv$$
$$=-\frac{H_\theta}{n}\left(\frac{\partial \phi}{\partial \xi}-\frac{\partial \phi}{\partial s}\frac{\partial z}{\partial \xi}\right)+\frac{\partial}{\partial \xi}\left(\frac{H_\theta}{n}\mathcal{F}_u^\xi\right)+\frac{\partial}{\partial \eta}\left(\frac{H_\theta}{m}\mathcal{F}_u^\eta\right)+\frac{\partial}{\partial s}\left(\frac{1}{mn}\mathcal{F}_u^s\right), \quad (6)$$

$$\frac{\partial}{\partial t}\left(\frac{H_\theta}{mn}v\right)+\frac{\partial}{\partial \xi}\left(\frac{H_\theta}{n}uv\right)+\frac{\partial}{\partial \eta}\left(\frac{H_\theta}{m}v^2\right)+\frac{\partial}{\partial s}\left(\frac{H_\theta}{mn}\Omega v\right)$$
$$+\left\{v\frac{\partial}{\partial \xi}\left(\frac{1}{n}\right)-u\frac{\partial}{\partial \eta}\left(\frac{1}{m}\right)\right\}H_\theta u+\frac{H_\theta}{mn}fu$$
$$=-\frac{H_\theta}{m}\left(\frac{\partial \phi}{\partial \eta}-\frac{\partial \phi}{\partial s}\frac{\partial z}{\partial \eta}\right)+\frac{\partial}{\partial \xi}\left(\frac{H_\theta}{n}\mathcal{F}_v^\xi\right)+\frac{\partial}{\partial \eta}\left(\frac{H_\theta}{m}\mathcal{F}_v^\eta\right)+\frac{\partial}{\partial s}\left(\frac{1}{mn}\mathcal{F}_v^s\right). \quad (7)$$

Balance of energy:

$$\frac{\partial}{\partial t}\left(\frac{H_\theta}{mn}T\right)+\frac{\partial}{\partial \xi}\left(\frac{H_\theta}{n}uT\right)+\frac{\partial}{\partial \eta}\left(\frac{H_\theta}{m}vT\right)+\frac{\partial}{\partial s}\left(\frac{H_\theta}{mn}\Omega T\right)$$
$$=\frac{\partial}{\partial \xi}\left(\frac{H_\theta}{n}\mathcal{F}_T^\xi\right)+\frac{\partial}{\partial \eta}\left(\frac{H_\theta}{m}\mathcal{F}_T^\eta\right)+\frac{\partial}{\partial s}\left(\frac{1}{mn}\mathcal{F}_T^s\right). \quad (8)$$

The balance equation for a passive tracer could be formulated in exactly the same form as the energy equation. The "vertical velocity" in s-coordinates, Ω, is defined as

$$\Omega=\frac{1}{H_\theta}\left(w-mu\frac{\partial z}{\partial \xi}-nv\frac{\partial z}{\partial \eta}\right). \quad (9)$$

Hydrostatic pressure balance:

$$\frac{\partial \phi}{\partial s}=-\left(\frac{H_\theta g\rho}{\rho_0}\right). \quad (10)$$

Equation of state:

$$\rho=\rho(p,T,S). \quad (11)$$

For the equation of state (11), a representation suggested by Bührer and Ambühl [2] (with no dependence on depth and salinity) has been used.

The turbulent fluxes $\mathcal{F}_\varphi^i$ have been formulated by gradient laws. They can be written in s-coordinates for a representative variable φ (either u, v, or T) as

$$\mathcal{F}_\varphi^\xi=D_H^{(\varphi)}m\left(\frac{\partial \varphi}{\partial \xi}-H_\theta\frac{\partial z}{\partial \xi}\frac{\partial \varphi}{\partial s}\right),$$
$$\mathcal{F}_\varphi^\eta=D_H^{(\varphi)}n\left(\frac{\partial \varphi}{\partial \eta}-H_\theta\frac{\partial z}{\partial \eta}\frac{\partial \varphi}{\partial s}\right), \quad (12)$$
$$\mathcal{F}_\varphi^s=-m\frac{\partial z}{\partial \xi}\mathcal{F}_\varphi^\xi-n\frac{\partial z}{\partial \eta}\mathcal{F}_\varphi^\eta+D_V^{(\varphi)}\frac{1}{H_\theta}\frac{\partial \varphi}{\partial s}.$$

The free surface enters the problem through the vertical integration of Eqs. (5), (6), and (7). Assuming that the vertically integrated transport is divergence-free (equivalent to the rigid-lid assumption) the integrated equations can be combined into one elliptic equation for the streamfunction ψ (see, e.g., Simons [21]).

Due to the presence of fast barotropic gravity waves, models that do not use a rigid-lid formulation either employ a mode-splitting technique as described in Song and Haidvogel [22] or introduce the free surface via an implicit method (see, e.g., Casulli and Cheng [4], Dukowicz and Smith [6]). Since mixing and convection processes in lakes and reservoirs are hardly influenced by fast barotropic gravity waves and since the rigid-lid assumption does not filter any topographic Rossby waves, which do contribute to advection, we decided to make use of a the rigid-lid formulation.

With the definition of the streamfunction ψ,

$$\begin{aligned} \bar{u} &= -\left(\frac{n}{H_\theta}\right)\frac{\partial \psi}{\partial \eta}, \\ \bar{v} &= \left(\frac{m}{H_\theta}\right)\frac{\partial \psi}{\partial \xi}, \end{aligned} \tag{13}$$

the barotropic part of the problem may be described by

$$\frac{\partial}{\partial t}\left\{\left(\frac{m}{nH_\theta}\right)\frac{\partial^2 \psi}{\partial \xi^2} + \left(\frac{n}{mH_\theta}\right)\frac{\partial^2 \psi}{\partial \eta^2} + \left(\frac{m}{nH_\theta}\right)\frac{\partial \psi}{\partial \xi} + \left(\frac{n}{mH_\theta}\right)\frac{\partial \psi}{\partial \eta}\right\} = \bar{\mathcal{R}}. \tag{14}$$

For the exact form of the integrated right hand side $\bar{\mathcal{R}}$ and details of the derivation see Güting [10].

In the above equations the following notation, if not defined in the text, has been used:

u, v, w	ξ, n, and z components of the velocity
$\bar{u}, \bar{v}$	vertically integrated velocity components
ψ	streamfunction of the vertically integrated velocity
T	temperature
ρ	density
ϕ	dynamic pressure
f	Coriolis parameter ($f = \Omega_{\text{earth}} \sin(\text{lat})$)
g	acceleration due to gravity
φ	dummy variable, either u, v, or T
$D_V^{(\varphi)}$	vertical turbulent difusivity
$D_H^{(\varphi)}$	horizontal turbulent diffusivity

At the bottom ($s = -1$) and at the surface ($s = 0$) flux boundary conditions of the form

$$\frac{1}{H_\theta} D_V^{(\boldsymbol{u})} \frac{\partial \boldsymbol{u}}{\partial s} = \boldsymbol{\tau}, \qquad \frac{1}{H_\theta} D_V^{(T)} \frac{\partial T}{\partial s} = q^{(T)} \tag{15}$$

have to be satisfied. In our case the normal heat flows $q^{(T)}$ at all boundaries have been set equal to zero. We have chosen for the wind shear a quadratic, and for the bottom friction a linear, relationship of the form

$$\boldsymbol{\tau}^{\text{surf}} = \rho_{\text{wind}} C_D |\boldsymbol{u}_{\text{wind}}| \boldsymbol{u}_{\text{wind}}, \tag{16}$$

$$\boldsymbol{\tau}^{\text{btm}} = \rho_{\text{water}} \gamma_h \boldsymbol{u}_{\text{water}}, \tag{17}$$

where C_D is the wind drag coefficient and γ_h is the bottom friction coefficient. At the lateral model boundaries all fluxes equal zero and no friction has been assumed.

3. NUMERICAL METHOD

3.1. *Vertical Discretization*

Both models use the same FD discretization in the horizontal direction but they differ completely in the vertical direction: Model A is based on a centered FD method, whereas model B uses Chebyshev polynomials $P_k(\sigma)$ to approximate a variable φ in a spectral way. The following table shows how the vertical derivatives are expressed in both models:

Model A (FD)	Model B (SP)
(s-coordinates)	(σ-coordinates)
	$\varphi_n = \varphi(\sigma_n) \approx \sum_{k=0}^{N} P_k(\sigma_n)\hat{\varphi}_k$
$\left.\dfrac{\partial\varphi}{\partial s}\right\|_{s_n} \approx \dfrac{\varphi(s_n+\Delta s)-\varphi(s_n-\Delta s)}{2\Delta s}$	$\left.\dfrac{\partial\varphi}{\partial\sigma}\right\|_{\sigma_n} \approx \dfrac{\partial P_k(\sigma_n)}{\partial\sigma}\hat{\varphi}_k$
	$= R_{nk}F_{kl}^{-1}\varphi_l = C_{nl}\varphi_l$
	with: $F_{nk} = P_k(\sigma_n)$
	and: $R_{nk} = \dfrac{\partial P_k(\sigma_n)}{\partial\sigma}$

In model B the $\hat{\varphi}_k$ are the polynomial coefficients that are recovered from the collocation point values φ_k by a linear matrix transformation. The vertical collocation points σ_n in the spectral method are chosen to be the positions of extrema of the highest order Chebyshev polynomial leading to a higher resolution near the top and the bottom. In contrast, model A uses evenly spaced, centered finite differences. In this case a higher resolution near the top and the bottom can only be achieved by the use of the nonlinear s-coordinates with the control parameters θ and b.

It is clear that in model A a vertical derivative of a variable at the collocation point n only depends on the value of the two points next to it but that in model B it involves *all* values. This means that, in general, for each vertical implicit time step in model B a fully occupied matrix has to be inverted.

3.2. *Time Stepping*

Using Eq. $(12)_3$, Eqs. (6), (7), and (8) may be rewritten with the generic variable φ as

$$H_\theta \frac{\partial\varphi}{\partial t} = \underbrace{\frac{\partial}{\partial s}\left(\frac{1}{H_\theta}D_V^{(\varphi)}\frac{\partial\varphi}{\partial s}\right)}_{\mathcal{D}} \underbrace{- \frac{\partial}{\partial s}(H_\theta\Omega_\varphi) + \frac{\partial}{\partial s}\left(-m\frac{\partial z}{\partial\xi}\mathcal{F}_\varphi^\xi - n\frac{\partial z}{\partial\eta}\mathcal{F}_\varphi^\eta\right) + mn\mathcal{R}}_{\mathcal{R}^*}, \quad (18)$$

where $\mathcal{R}$ is the sum of all other terms. The models have been modified[1] to allow for two kinds of semi-implicit time stepping procedures (see Wang and Hutter [26]) to remove the

[1] During the modification a bug in the original SPEM5.1 implicit time stepping scheme was discoverd. The improved code is now available for all users as a new patch level.

severe stability condition on the vertical diffusion terms due to the very small vertical grid size near the lateral boundaries. Provided is either a second-order Crank–Nicolson scheme that, with the abbreviations introduced in Eq. (18), can be written as

$$H_\theta \varphi^{t+\Delta t} = H_\theta \varphi^{t-\Delta t} + \Delta t (D^{t+\Delta t} - D^{t-\Delta t}) + 2\Delta t mn \mathcal{R}^{*,t}, \tag{19}$$

or a simple backward Euler scheme of first order,

$$H_\theta \varphi^{t+\Delta t} = H_\theta \varphi^{t-\Delta t} + 2\Delta t D^{t+\Delta t} + 2\Delta t mn \mathcal{R}^{*,t}. \tag{20}$$

Both schemes perform the implicit time step only for the diffusive term $\mathcal{D}$ so as to remove the most severe time step limitation. The resulting linear system involves the solution of a tridiagonal matrix for model A and a fully occupied matrix in model B. The time step for the term $\mathcal{R}^*$ is an explicit Leapfrog scheme. Thus further s-derivatives arising from the vertical advection term (the first term in $\mathcal{R}^*$) and the flux corrections induced by the s-coordinates (second term) will be treated explicitly. For a very small vertical grid size these terms may influence the stability. The same is true for a very small horizontal grid size when the maximum time step is delimited by the stability criterion associated with the explicit scheme for the horizontal diffusion terms. We will show that both effects play an important role for stability in our calculations.

4. USING OCEAN MODELS FOR LAKES

Many three-dimensional models used in physical limnology have been designed like SPEM for the simulation of ocean circulation. SPEM has been successfully applied to many oceanographical problems but due to the smaller length scales of lakes compared to the scales of the ocean the model could not be used in limnology until a vertical implicit time stepping had been implemented. However, even with this semi-implicit time stepping there are still further effects that are only of peripheral significance in oceanography but restrict the stability in limnology:

- The influence of the explicit scheme for horizontal diffusion terms on stability. These terms are treated explicitly in almost all models since an implicit scheme could be performed only at an extemely high cost.
- The influence of the (explicit) flux correction terms that only appear in σ-coordinate type models (e.g., the first and second terms on the right hand side of $(12)_3$). An implicit scheme on these terms could only be performed at a very high cost because they involve a combination of vertical s-derivatives and horizontal ξ-, η-derivatives. Wang and Hutter [25] showed that using an ADI method (with successive implicit time steps in the ξ-, η-, and s-directions) does not suffice in the case of lake simulation. They pointed out that the ADI method provided even less stability than a semi-implicit scheme in the vertical direction.

In contrast to this, in Cartesian models the flux correction terms do not appear, and *all* vertical derivatives may be treated implicitly (see, e.g., Casulli and Cattani [3]).

Figure 1 shows vertical slices of the s-coordinates with different parameters θ used in our calculations: The s-coordinate lines are compressed at the lateral model boundaries where the minimum depth has been set to $h_{\min} = 5$ m. This leads to a minimum vertical grid size of only 15 cm for $N = 30$ collocation points. In our calculations the maximum time step was reduced by a factor of three to five in the presence of the flux correction terms (e.g., the first and second terms on the right hand side of $(12)_3$). However, neglecting these terms

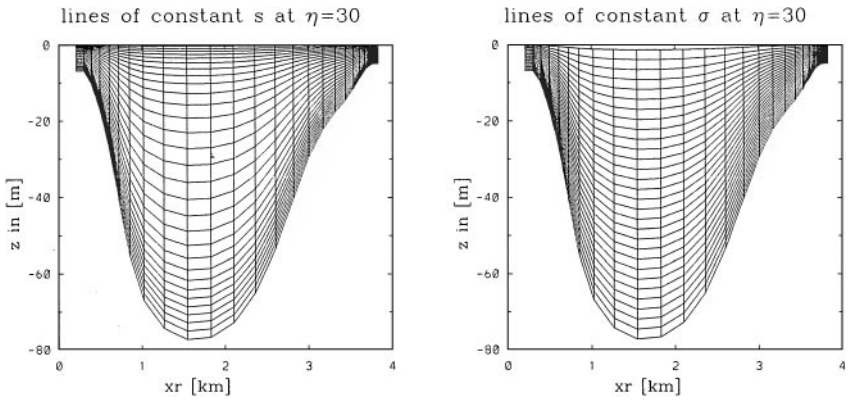

FIG. 1. Vertical slice at $\eta = 30$ (for orientation refer to Fig. 2) showing lines of constant s (with $\theta = 0.001$, corresponding to σ-coordinates, and with $\theta = 4$ and $b = 0.8$) in Lake Ammer.

would lead to a "horizontal" diffusion along surfaces of constant s instead of constant z. Our calculations showed that this causes only a small error in the barotropic case near regions of steep topography but a considerable error in the baroclinic (stratified) case.

5. ACCURACY, STABILITY, AND PERFORMANCE

5.1. *Error*

The convergence of each model and the difference between model A and model B have been analyzed in terms of a rms error. Since the horizontal discretizations in the two cases are identical[2] we introduce a local volume-weighted rms error for each vertical column of N data points:

$$\mathrm{rms}^{\varphi}_{\mathrm{loc}} = \sqrt{\frac{\sum_k^N \left(\varphi_k^{\mathrm{ref}} - \varphi_k\right)^2 \Delta V_k^{\mathrm{ref}}}{\sum_k^N \varphi_k^{\mathrm{ref}} \Delta V_k^{\mathrm{ref}}}}. \tag{21}$$

- φ_k^{ref} is the value at the reference collocation point k for a reference run (i.e., usually a run with very small grid size or time step)
- φ_k is the value of a run to be compared to the reference run interpolated to the reference collocation point k. The interpolation is performed either by linear interpolation (model A) or by Chebyshev polynomials (model B).
- $\Delta V_k^{\mathrm{ref}}$ is the reference volume assigned to the reference collocation point k.

A global measure of error may be introduced by defining an area-weighted global rms error averaged over $L \times M$ horizontal grid points.

$$\mathrm{rms}^{\varphi}_{\mathrm{glob}} = \sqrt{\frac{\sum_{i,j}^{L\cdot M} \left\{\left(\mathrm{rms}^{\varphi}_{\mathrm{loc}}\right)_{i,j}\right\}^2 \Delta A_{i,j}}{\sum_{i,j}^{L\cdot M} \Delta A_{i,j}}}, \tag{22}$$

where $\Delta A_{i,j}$ are the areas assigned to the horizontal grid points.

[2] The horizontal averaging scheme for the Coriolis term was different in the original model B, leading to a considerable error near some boundaries where the grid was coarse. We used the averaging procedure from model A for both models.

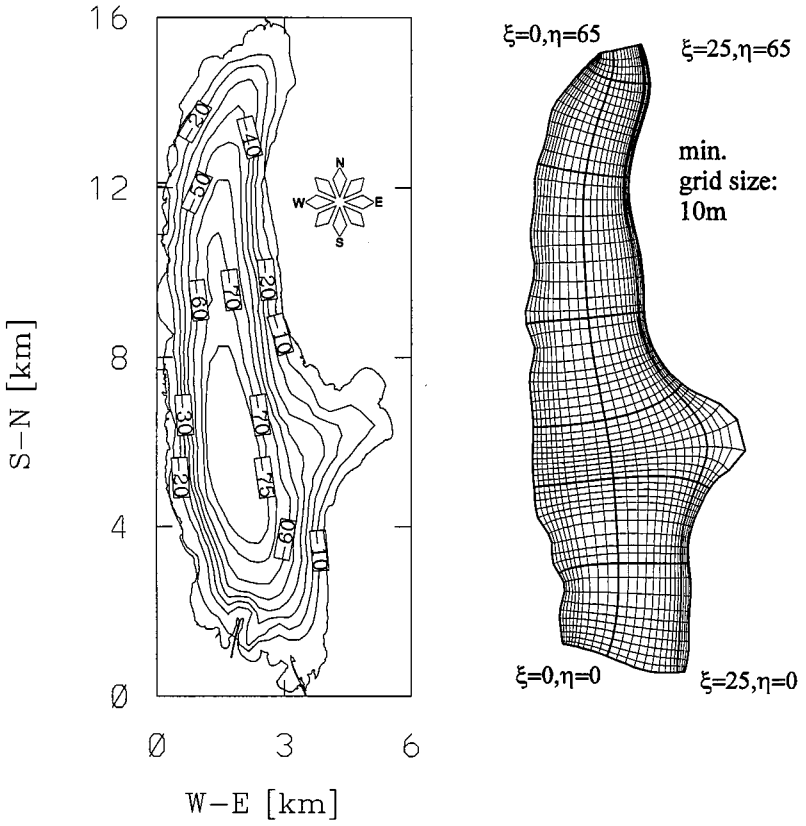

FIG. 2. The topography of Lake Ammer (left) and the horizontal orthogonal grid (right).

5.2. *Parameters*

Model A and model B have been run for both a rectangular basin with constant depth ($12{,}500 \times 3000 \times 40$ m) and for Lake Ammer (for the topography and horizontal grid see Fig. 2). The parameters used for all runs are shown in Table I.

5.3. *Stability*

To our knowledge the stability of the scheme employed in this model or in similar nonlinear models using coordinate transforms has not been fully explored. Casulli and Cattani

TABLE I
Parameters Common in All Calculations

Parameter	Lake Ammer and rect. basin
Drag coefficient C_D	1.5×10^{-3}
Bottom friction coeff. γ_h	10^{-3} ms^{-1}
Coriolis parameter	1.08×10^{-4} s^{-1}
Windspeed	3 ms^{-1} from South
Horizontal resolution	25×65 (see Fig. 2)
Maximum depth	82 m (L. Ammer)

Note. For other parameters see the main text.

[3] claimed to show stability of their FD method on a Cartesian grid using the von Neumann method only for a linearized version of the shallow water equations in an infinite domain. Gal-Chen and Sommerville [8] gave a general derivation of the primitive equations for topographical coordinates and found by numerical evidence that their scheme was stable whenever its analogous Cartesian scheme was stable. In a heuristic way they derived bounds for the time step, the grid size, and the Jacobian of the transformation for stability (see Gal-Chen and Sommerville [7]). We want to underline our experimental stability analysis by heuristic arguments in a very similar manner.

Let us recall from Section 4 that, with a vertical implicit time stepping, stability is mainly affected by the explicit treatment of the horizontal diffusion terms and the flux correction terms arising from the σ-type coordinates. The stability condition related to the horizontal diffusion problem is dominated by the properties of an explicit Euler scheme on the typical terms

$$\frac{\partial}{\partial t}\left(\frac{H_\theta}{mn}\varphi\right) = \frac{\partial}{\partial \xi}\left(\frac{H_\theta}{n} D_H^{(\varphi)} m \frac{\partial \varphi}{\partial \xi}\right) + \frac{\partial}{\partial \eta}\left(\frac{H_\theta}{m} D_H^{(\varphi)} n \frac{\partial \varphi}{\partial \eta}\right) + \cdots. \tag{23}$$

Using the estimates

$$\frac{1}{m}\frac{\partial}{\partial \xi} \approx \frac{\partial}{\partial x}, \qquad \frac{1}{n}\frac{\partial}{\partial \eta} \approx \frac{\partial}{\partial y} \tag{24}$$

and assuming $D_H^{(\varphi)}$ to be constant, the terms (23) can be shown to correspond to the horzional diffusion problem in Cartesian coordinates

$$\frac{\partial \varphi}{\partial t} = D_H^{(\varphi)}\left(\frac{\partial^2 \varphi}{\partial x^2} + \frac{\partial^2 \varphi}{\partial y^2}\right). \tag{25}$$

Hence an explicit Euler scheme for (23) with centered finite differences of comparable grid spacing in both directions will be subject to the well known stability condition

$$\Delta t_{\max} = \text{const} \frac{(\Delta x_{\min})^2}{2 D_H^{(\varphi)}}, \tag{26}$$

where $x_{\min}$ denotes the smallest horizontal grid spacing and const is a constant of order 1. Clearly, such an estimate neglects nonlinear and coupling effects and, moreover, is only justified if the Jacobian of the transformation is close to 1. However, it shows some aspects of the relation between the physical and the mapped domain and provides a rough estimate for the maximum time step. We found that stability cannot always be forced by a very small diffusivity D, since a minimum of explicit smoothing is always required. In both models this smoothing can be greatly reduced by choosing the diffusivity in such a way that all relevant oscillations can still be observed (see Section 6).

Table II shows the maximum possible size of the time step for models A and B in different situations. With selected numbers of vertical collocation levels the two models achieve comparable accuracy (see Section 5.4). To check the models for the influence of the vertical derivatives on stability we observed the variation of the maximum time step with varying vertical grid spacing. To check for the influence of the horizontal diffusion terms we varied the horizontal diffusion and observed the change in the maximum time step due to the stability criterion for the explicit scheme.

Since the rectangular basin has a uniform depth no flux correction terms (first and second terms on the right hand side of $(12)_3$) are involved and stability can only be related to the

TABLE II
Stability Performance of Models A ($N = 30$ Collocation Levels) and B ($N = 6$ Collocation Levels) for a Non-stratified Fluid

Max. time step	Model A (CN)	Model B (CN)	Model B (Euler)
Rectangle	1600 s	1800 s	5800 s
Lake Ammer	90 s	180 s	190 s

Note. The diffusivities were set equal to $D_V = 0.01\ \mathrm{m^2\ s^{-1}}$ and $D_H = 0.3\ \mathrm{m^2\ s^{-1}}$ throughout the domain. (CN = Crank–Nicolson.)

minimum horizontal grid spacing of $\Delta x_{\min} \approx 100$ m. The first line in Table II shows that, as expected, the models have comparable maximum time steps for the same time-stepping scheme (e.g., Crank–Nicolson). However, with the backward Euler scheme a considerably larger time step can be achieved, which is assumed to be due to a larger dissipative term introduced by the Euler scheme. A von Neumann stability analysis of the one-dimensional diffusion problem shows indeed that the dissipative error of the backward Euler scheme is always larger than that of the Crank–Nicolson scheme. Since in both cases the amplification factor for the diffusion problem is real none of the methods exhibits a phase error.

In Lake Ammer the minimum vertical grid size is about 15 cm for the FD model (30 evenly spaced collocation levels) and 30 cm for the spectral model (6 collocation levels, not evenly spaced) and the minimum horizontal grid size is about 10 m. The second line in Table II shows the stability performances of both models without the flux correction terms in the non-stratified case. Due to the small horizontal and vertical grid spacings the maximum time step is reduced and model B proves to be more stable, almost independently of the time-stepping scheme used. It is interesting that model A always exhibits some sensitivity of the maximum time step on a variation of the vertical diffusion, even though both time-stepping schemes should be unconditionally stable. Apparently, the scheme exhibits the influence of nonlinear terms and a coupling of the one-dimensional vertical diffusion scheme to the horizontal discretization.

Table III shows that apart from the above the flux correction terms exert a great influence: For a vertical resolution of $N = 30$ we tested stability for constant vertical diffusivities in the physically interesting range $0.001\ \mathrm{m^2\ s^{-1}} \le D_V \le 0.05\ \mathrm{m^2\ s^{-1}}$. The presence of the correction terms reduced the time step by a factor of three. For $D_H = 1\ \mathrm{m^2\ s^{-1}}$ stability could only be achieved for a very small time step of 10 s whereas for $D_H = 0.1\ \mathrm{m^2\ s^{-1}}$ all runs remained stable for a time step of 60 s in the non-stratified case.

The same tests performed in the case of a stratified fluid according to Fig. 8 give a very different picture. For an acceptable accuracy (corresponding to a vertical resolution of

TABLE III
Stability of Model A for a Series of Test Runs with $0.001\ \mathrm{m^2\ s^{-1}} \le D_V \le 0.05\ \mathrm{m^2\ s^{-1}}$ in the Non-stratified Case for Different Values of D_H

D_H	60 s	30 s	10 s
1.0	Unstable	Unstable	Stable
0.3	Unstable	Stable	Stable
0.1	Stable	Stable	Stable

$N = 55$ in model A, see Fig. 4), stability required a small maximum time step of $\Delta t = 10$ s. For an identical problem and time step model B performed stable runs only for a small window of vertical spectral collocation points between $N = 30$ and $N = 40$. Plots of the vertical distribution of some model variables showed that large oscillations of the Chebyshev polynomals at the bottom of the mixed layer induce instabilities. Obviously the spectral model B suffers from the inability to represent a stratification common in lakes during the summer. This fact of course strongly limits the use in lake modelling.

5.4. *Accuracy*

We compared the convergence of both models by means of the rms error of the velocity fields according to Eq. (22). The values at the collocation points of model B were interpolated to the collocation points of model A by Chebyshev polynomials if necessary. The reference runs had vertical resolutions of $N = 60$ in model A and $N = 20$ in model B; the reference time step was always 10 s.

From the theory of spectral methods (see, e.g., Gottlieb and Orszag [9]) one would expect a very fast convergence for model B with an increasing number N of vertical collocation levels. For a sufficiently smooth solution the error for the spectral model should decrease faster than any finite power of N, whereas for the FD model B it should be proportional to N^{-2}.

As shown in Fig. 3 this behavior is basically corroborated by the numerical models in the non-stratified case. It also can be seen that the convergence properties for the rectangular basin and for Lake Ammer are almost identical. The effect of the control parameters θ and b was small in the non-stratified case (compare FD1 and FD2 in the right panel). As mentioned in Section 5.3, in the stratified case model B was not able to produce stable runs over a large range of vertical collocation points and thus convergence could only be certified by comparing it with that of model A. The behavior of this model is documented in Fig. 4

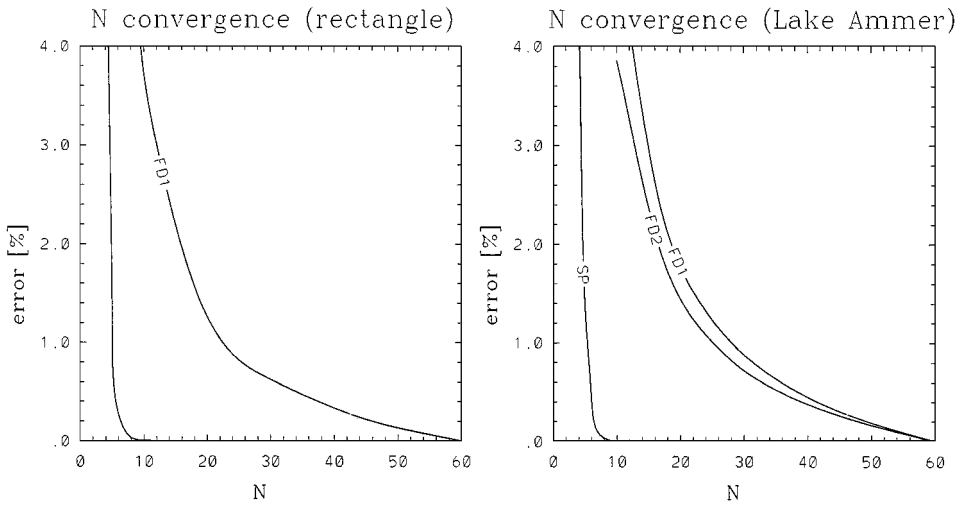

FIG. 3. Global rms error of the velocity field with increasing number N of vertical collocation points for the rectangular basin (left) and for Lake Ammer (right). For the spectral model B (SP) the reference N (error $\equiv 0\%$) was chosen to be 20, for the finite difference model A (FD1 and FD2) the reference N was 60. The time step was 10 s, causing only a negligible error. FD1 was a run with $\theta = 0.001$, corresponding to linear σ-coordinates; FD2 was a run with $\theta = 4$, $b = 0.8$ (refer to Fig. 1).

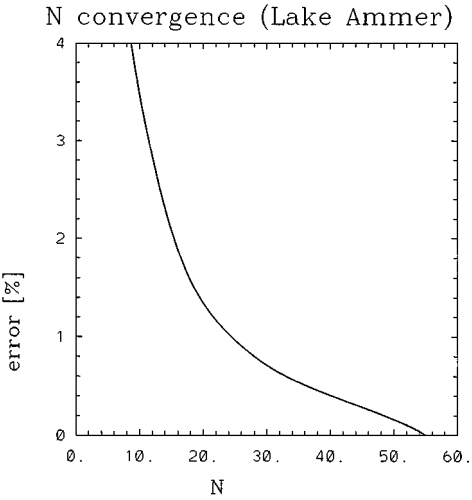

FIG. 4. Global rms error of the velocity field in the stratified case according to Fig. 8 with an increasing number of N vertical grid points for Lake Ammer. The reference N was 55. The time step was 10 s.

and it is seen that there are no fundamental differences from the model's behavior in the non-stratified case.

From Fig. 3 (right) a vertical minimum resolution of $N = 30$ for model A and $N = 6$ for model B can be determined for a moderate global error of less than 1%. Clearly, for an explicit time-stepping scheme model B is superior, if comparable maximum time steps are assumed for the two models. (In fact model B is always more stable in a non-stratified fluid.)

For an implicit time-stepping scheme convergence with decreasing Δt is shown in Fig. 5 (left). Clearly the Crank–Nicolson scheme gives better results because of its quadratic convergence properties. However, as shown in Table II, the backward Euler scheme is

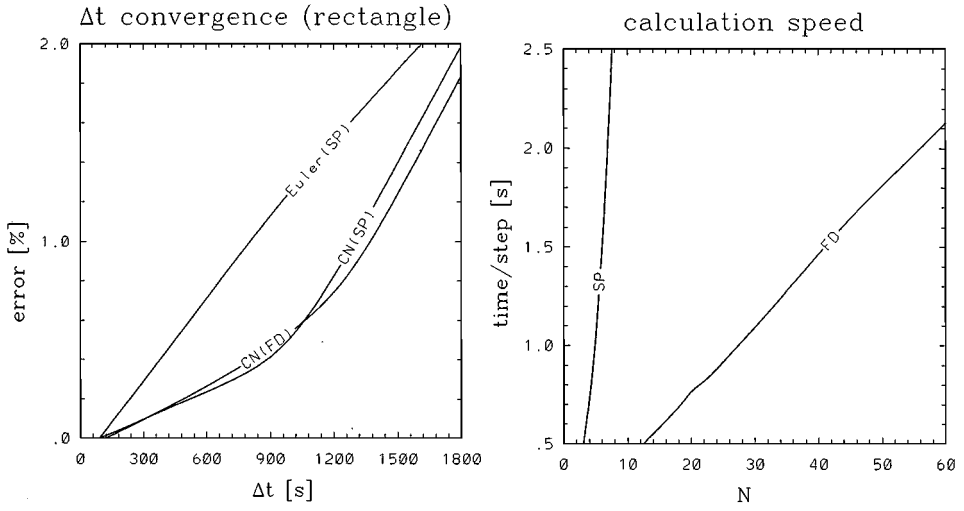

FIG. 5. Global rms error of the velocity field with decreasing Δt in a rectangular basin for model A (FD) and model B (SP) with either a backward Euler or a Crank–Nicolson (CN) scheme (left). (For the reference run (error $\equiv 0\%$): $N = 60$ and $\Delta t = 10$ s). The right panel shows the time required for one time step on a pentium computer.

more stable under some conditions and the maximum time step required for stability for lake simulations is usually so small that moderate accuracy requirements are satisfied with either scheme. It follows that the time-stepping scheme should be chosen primarily in conjunction with stability considerations.

Figure 5 (right) shows the time required for one implicit time step on a pentium computer for both models in the non-stratified case. This picture reveals a great disadvantage of the spectral model: For each implicit time step, in general, a fully occupied matrix must be inverted, leading to an integration time that grows quadratically with increasing grid resolution N, whereas in the FD model only a tridiagonal matrix has to be inverted. For a global error of 1% ($N = 6$ SP, $N = 30$ FD) the integration CPU time for one time step was 1.1 s for the FD model and 1.5 s for the spectral model. Of course these values depend greatly on the properties of the linear solver and the machine architecture. The actual calculation time for a particular simulation depends on both the integration time for one time step and the maximum time step size, which may be delimited as shown in the above by accuracy (rectangle) or by stability (Lake Ammer). With a maximum time step for Lake Ammer from Table II of 190 s for the spectral model and 90 s for the FD model the actual calculation time for the spectral model is faster by a factor of $\approx$1.5. Clearly, this result is no longer valid in the stratified case. As discussed in Section 5.3 with model B the minumum number of vertical collocation points was 30 for a stable run and no economical integration of the shallow water equations was possible for Lake Ammer.

We want to point out the fact that the above test provides only a rough estimate that depends on a number of factors like smallest grid size, error requirements, machine architecture, and solver.

It may seem from the above that, in the non-stratified case, the spectral model B is slightly superior in stability and accuracy. However, we found that the Chebyshev polynomials show high sensitivity to the large gradients in the thermocline, leading to instabilities and negative diffusivities in the k-ϵ-model and thus violating the entropy inequality (see Güting [10]). This seems to be a crucial disadvantage of the spectral model from a practical point of view.

Having checked the convergence properties of models A and B we compared the two models. Both models were run with a very high resolution ($N = 60$ for model A, $N = 20$ for model B in the non-stratified case, and $N = 30$ with stratification) and a very small time step of 10 s. The values from model B were interpolated to the collocation points of model A by Chebyshev polynomials. We found that the local rms error, according to Eq. (21), between the two models was at all points less than 1%. This shows that both models reliably solve the shallow water equations.

5.5. *Conservation Properties*

Both models conserve the first moments of u, v, and T. This is due to a centered discretization of the conservative form of the shallow water equations as given in Eqs. (5)–(8) (see, e.g., Hirsch [14, pp. 237–241]). The same argument applies as well to the discretization of the vertical advection and diffusion terms in the FD model A, but not to the spectral vertical representation of model B. In that case conservation of the first moments is achieved by computing the vertical integral of a typical vertical advection term

$$\mathcal{A}_{\varphi I} = \int_{-1}^{0} \mathcal{A}_{\varphi}\, ds, \tag{27}$$

where

$$\mathcal{A}_\varphi = \frac{\partial}{\partial \sigma}\left(\frac{H_\theta \Omega \varphi}{mn}\right), \qquad \varphi = u, v, T \tag{28}$$

and then correcting the vertical advection term by

$$\mathcal{A}_{\varphi c} = \mathcal{A}_\varphi - \mathcal{A}_{\varphi I}. \tag{29}$$

Since this scheme has been found to have troublesome side effects (see Hedstrom [13]) the current correction is based on subtracting a second-order polynomial, which is zero at the top and the bottom, and has the same vertical integral as $\mathcal{A}_{\varphi I}$.

The conservation of mass is obviously satisfied by the boundary condition $\psi = \text{const}$ in Eq. (14), which is identical to stating that there is no overall mass flux through the boundaries.

6. RESULTS

6.1. *Barotropic Response*

In this section we consider the response of the homogeneous Lake Ammer to a Heaviside wind force from South. For the model runs the parameters shown in Table I were used. The horizontal momentum diffusion was assigned a constant value of $D_H = 0.3$ m^2 s^{-1}, the vertical momentum diffusion a value of $D_V = 0.01$ m^2 s^{-1}. The models were integrated over a period of 3 days. Since the equations are subject to the rigid-lid assumption (see Eq. (14)) no other waves except inertial and topographic waves can exist. The long periods of topographic waves cannot be recognized in a period of 3 days so that one would expect only the existence of an inertial oscillation far from the boundaries with a period of $T_i = 2\pi/f = 16.16$ h (see Hutter [15]).

Figure 6 (left) shows this oscillation, which is damped almost completely after 3 days. Figure 6 (right) shows the existence of a stationary Ekman layer with the characteristic

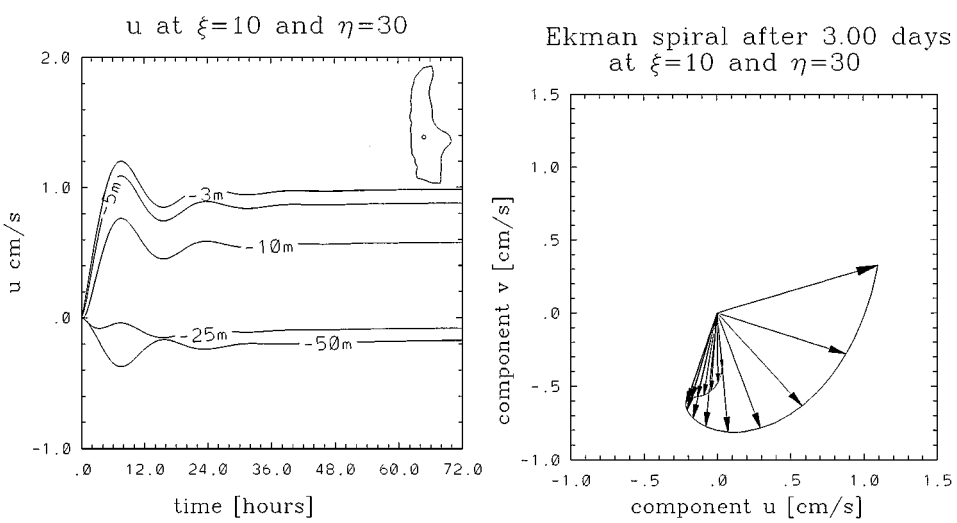

FIG. 6. The u component of the velocity (left) in the middle of L. Ammer (see position label in the upper right corner) at depths of 3, 5, 10, 25, and 50 m. The wind blows from south with 3 m s^{-1}; there is no density stratification. The panel on the right shows the vertical velocity profile after 3 days at the same point. Velocity vectors are drawn every 5 m starting at the surface. Computed by model A.

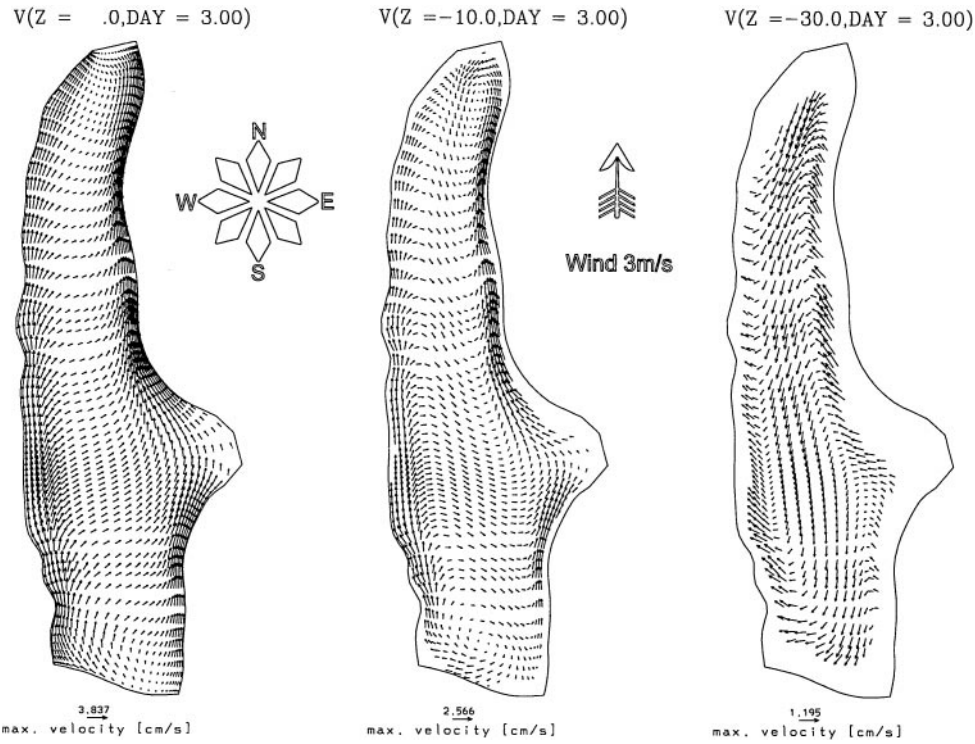

FIG. 7. Currents after a 3-day simulation of homogeneous Lake Ammer at depth levels of 0, 10, and 30 m (from left to right, observe the different scalings). Computed by model A.

clockwise rotation of the velocity vector down to a depth of 40 m. In deeper regions the flow can be regarded as completely geostrophic.

The steady-state currents for the barotropic case at several depth levels are given in Fig. 7, which shows the horizontal distribution of the velocity. In accordance with the general Ekman theory for deep waters (Simons [21]) the currents are dominated by a surface Ekman drift and an interior geostrophic flow. The mostly geostrophic longshore transport causes the most striking feature of the field: the nearshore coastal jets at the eastern and western shores. The vertically integrated transport of the Ekman layer from west to east is balanced by a weak transverse geostrophic current in the opposite direction.

6.2. *Baroclinic Response*

During most of the year a temperature stratification prevails in Lake Ammer. In this case a vertical density profile due to Eq. (11) develops and more types of waves may be excited. The theory (Hutter [16]) predicts the existence of Kelvin- and Poincaré-type waves (a brief decription of those types is given in the Appendix). The integration time was only 3 days; thus the effects of internal topographic waves (with very long periods) will not be discussed here. We used the parameters given in Table I and a stratification of temperature and vertical diffusivity as displayed in Fig. 8.

Figure 9 (top) shows the longshore velocity at the midpoints of the eastern and western shores as a function of time. From the graphs one of the two main types of waves may be identified: The "seiching" with the first baroclinic mode of a period of $T_k \approx 25$ h is caused

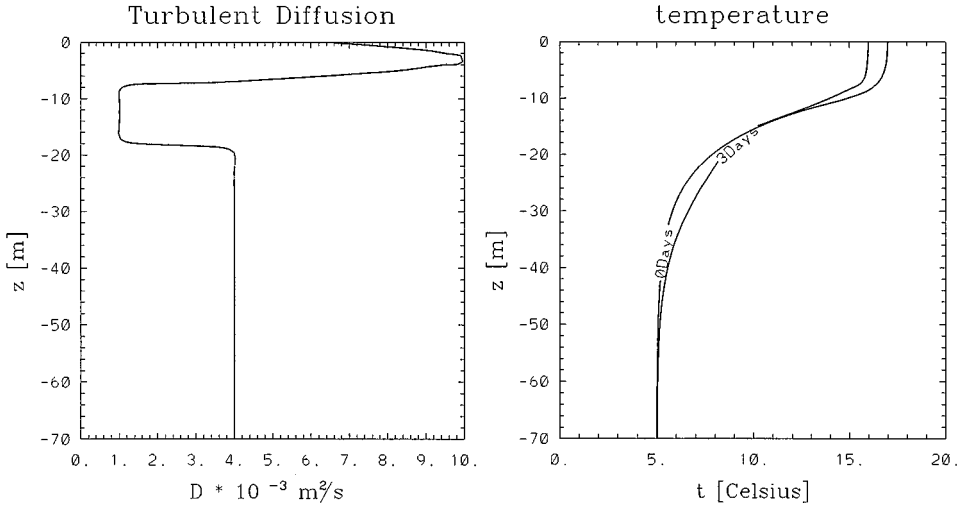

FIG. 8. Predefined stratification of vertical turbulent momentum diffusivity D_V (left) and the initial ("0 Days") and final ("3 Days") temperature stratification in the middle of Lake Ammer.

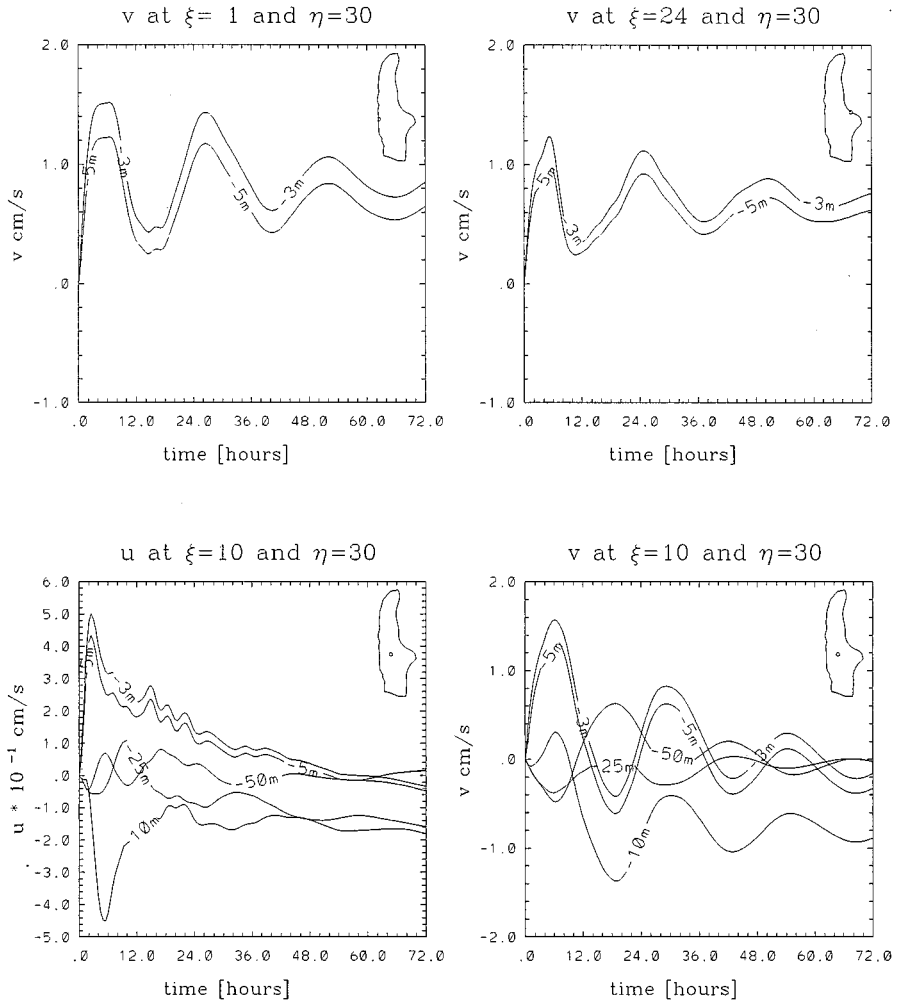

FIG. 9. The longshore component of the velocity (top) at the western and eastern shores at the depth levels 3 and 5 m. The bottom panels show the velocity in the middle of the lake at the depth levels 3, 5, 10, 25, and 50 m. Position labels are shown in the upper right corners of the plots. Computed by model A.

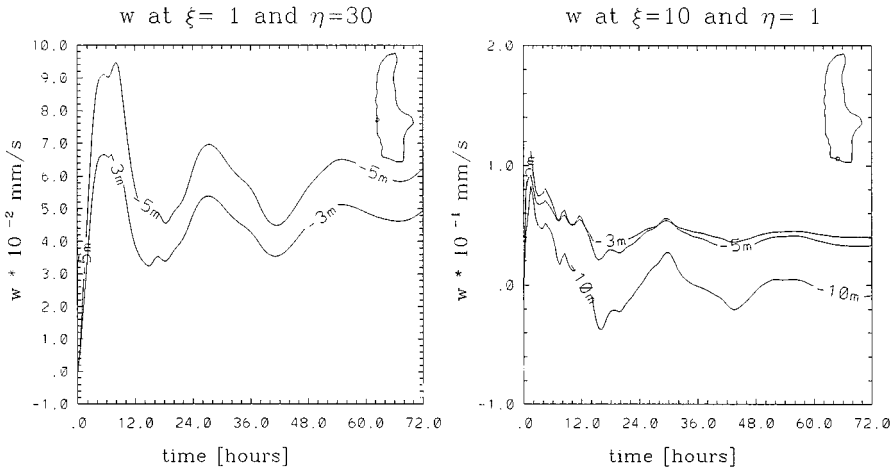

FIG. 10. The vertical component of the velocity at the western and southern shores at different depth levels shows upwelling. Observe the different scalings. Computed by model A.

by a superposition of two Kelvin-type waves circulating counterclockwise around the basin. Even though this kind of waves decays exponentially with the distance from the shore the oscillation can also be recognized in the middle of the lake (see Fig. 9, bottom) since the lake width is relatively small.

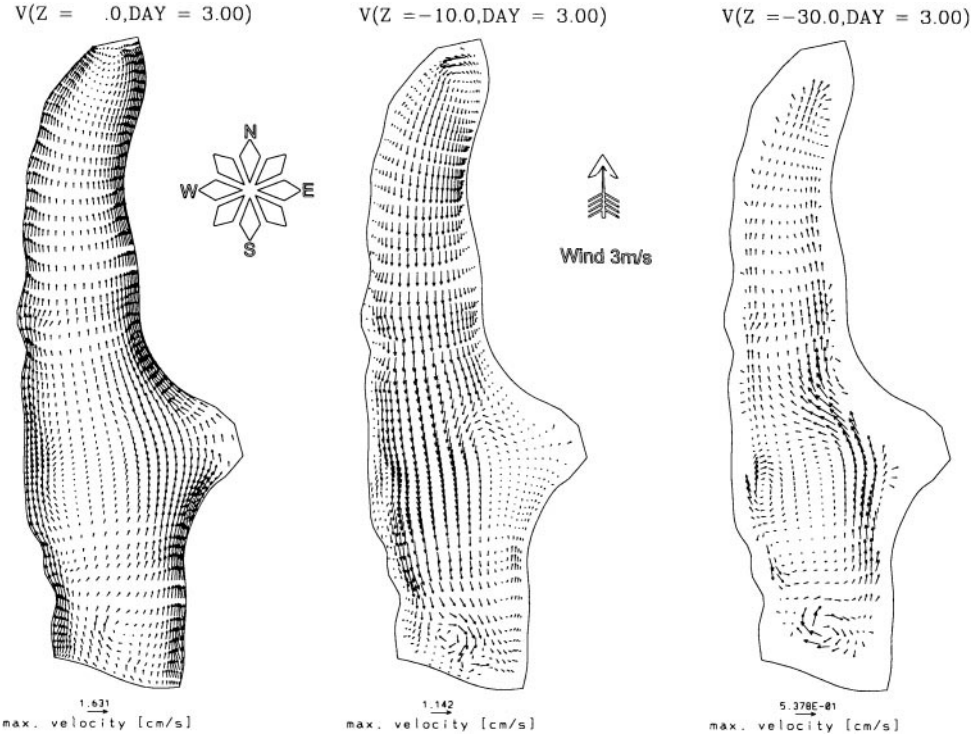

FIG. 11. Currents after 3 days of baroclinic simulation in L. Ammer at depth levels of 0, 10, and 30 m (from left to right). Computed by model A.

Evidence of the second, Poincaré-type waves, can be found in the whole basin. The lower left panel of Fig. 9 shows an oscillation in the transverse component of the velocity with a period $T_p \approx 3.75$ h in the middle of the lake that may be interpreted as a standing Poincaré-type wave. This oscillation can be found at almost all points of the basin.

The thermocline motion caused by the internal seiching leads to an upwelling at the southern and western shores and to a downwelling at the opposite shores. The upwelling can be clearly seen in Fig. 10, which shows a positive vertical velocity at the midpoints of the southern and western shores.

Horizontal slabs of the velocity profile after 3 days at different depths are given in Fig. 11. The picture shows that at the surface the velocity distribution deviates little from that of the barotropic situation. However, because the momentum diffusion increases with depth, at the first meters the surface flow rotation by the Coriolis force is much weaker and the flow is mainly in the direction of the wind. Again the development of coastal jets can be observed (see, e.g., Csanady [5]).

Figure 9 (bottom right) indicates that after 3 days the hypolimnetic oscillation has come to an end and the thermocline must have tilted sufficiently to set up a hydrostatic pressure gradient, which just balances the surface stress. At this stage of the motion the hypolimnion no longer balances the surface flow by a motion in the reverse direction. Thus the motion changes from a whole basin circulation to two closed vertical gyres, one each in the hypolimnion and the epilimnion, and the counterflow occurs in the metalimnion, as displayed in Fig. 11 (middle).

7. CONCLUSIONS

We compared two methods for the solution of the shallow water equations: a semi-spectral method and a traditional finite difference method. For a sufficiently fine grid the results of the two models agreed very well. This can be taken as an indication that each model reliably solves the primitive equations. We found that due to its very fast convergence with increasing vertical grid resolution the spectral method was superior in connection with an explicit time-stepping scheme, but with an implicit scheme, which is always required in lake modelling, we found the two methods to be comparable in calculation speed in the non-stratified case. However, due to the high sensitivity of the Chebyshev polynomials to sharp gradients near the thermocline (leading to instabilities and negative diffusivities in a k-ϵ-closure) the use of the spectral method is very restricted in the modelling of lakes with a strong summer stratification. In addition, the relative simplicity of the code for the FD model A compared to the code for the spectral model B should be viewed as another advantage of model A.

We pointed out that the s-coordinates provide a high degree of smoothness at the boundaries and thus make it possible to easily impose the boundary conditions and to work with very small diffusivities in order to observe all important wave types. This may be regarded as the greatest advantage of σ-type models over Cartesian models, which have to cope with a complicated interpolation of the physical boundary condition on the numerical grid, often leading to singularities near corner points (see Gal-Chen and Sommerville [8]) and spurious effects like convection and upwelling as described in Veronis [24].

A disadvantage common to all σ-type coordinate systems, however, is the introduction of additional flux correction terms that cannot be treated implicitly at an acceptable cost

and thus restrict the maximum time step. Other effects mentioned in Marshall *et al.* [18] may play a role in the application of such models. Even though σ-type models proved to be a good choice for the modelling of large lakes (see, e.g., Güting and Hutter [11]) we think that the superiority of one model type over the other can only be certified for special cases. However, for small lakes that require a very small vertical and horizontal resolution the application of σ-type models seems to be somewhat restricted.

APPENDIX: KELVIN AND POINCARÉ WAVES

For small to medium size lakes rotational effects in gravity waves are usually manifested as modifications of the solutions in which the rotation of the Earth is ignored. To demonstrate this we consider the vertically integrated shallow water equations without friction of the form

$$\frac{\partial \zeta}{\partial t} + \left(\frac{\partial U}{\partial x} + \frac{\partial V}{\partial y} \right) = 0, \tag{30}$$

$$\frac{\partial U}{\partial t} - fV = -gh\frac{\partial \zeta}{\partial x}, \qquad \frac{\partial V}{\partial t} + fU = -gh\frac{\partial \zeta}{\partial y}, \tag{31}$$

where U and V are the vertically averaged velocities and ζ is the surface elevation. The barotropic modes are obtained by setting h equal to the water depth, and the baroclinic modes of a corresponding two-layer model by setting

$$h := h_i = \frac{\Delta\rho}{\rho}\frac{h_1 h_2}{h_1 + h_2}, \tag{32}$$

where $\Delta\rho$ is the density difference between a layer of thickness h_1 above the thermocline and a layer of thickness h_2 below the thermocline.

For a detailed description of the wave solutions presented below, see, for example, Hutter [16].

A.1. *Kelvin Waves*

It is our intention to construct solutions of (30) and (31) that enjoy a transverse variation of ζ in conformity with the Coriolis term. To this end we consider a half-infinite basin with constant depth and bounded at $y = 0$; we seek wave solutions of the form

$$u = u_0 h \Phi(y) e^{i(kx - wt)}, \qquad v := 0, \qquad \zeta = \zeta_0 \Phi(y) e^{i(kx - wt)}, \tag{33}$$

which satisfy the no-flux condition through the side boundary; a forteriori, it requires V to vanish everywhere in the half space. Substituion of (33) into (30) and (31) yields the dispersion relation

$$c = c_{ph} = \frac{\omega}{k} = \sqrt{gh}, \tag{34}$$

and the solutions

$$\Phi(y) = \exp\left\{ -\frac{f}{c} y \right\}, \qquad \zeta_0 = \frac{c}{g} u_0. \tag{35}$$

These solutions, named in honour of Lord Kelvin, will be modified in the presence of topography and will be called "Kelvin-type" waves by us.

A.2. *Poincaré Waves*

Kelvin waves have the property that the water particle motion is purely longitudinal. There are other wave solutions of (30) and (31) that satisfy the boundary condition $V = 0$ at the channel sides; however, they may have nontrivial transverse velocity inside the channel. Eliminating U and ζ from the equations and seeking plane wave solutions for V

$$v = V_0(y)e^{i(kx-\omega t)} \tag{36}$$

yield the eigenvalue problem

$$\frac{\partial^2 V_0}{\partial y^2} + \left(\frac{\omega^2 - f^2}{gh} - k^2\right)V_0 = 0, \qquad 0 \le y \le B \tag{37}$$

for the distribution of V across a channel with the boundary conditions $V_0 = 0$ at $y = 0$ and $y = B$ (see Hutter [16]). Equations (36) and (37) describe the Poincaré waves. The solution of (37) is

$$V_0 = \bar{V}\sin\left(\frac{m\pi}{B}y\right) \tag{38}$$

with the dispersion relation

$$k^2 = \frac{\omega^2 - f^2}{gh_n} - \frac{m^2\pi^2}{B^2} \qquad (m = 1, 2, 3, \ldots, n = 0, 1, 2, \ldots) \tag{39}$$

or alternatively

$$\omega^2 = f^2 + gh_n\left(k^2 + \frac{m^2\pi^2}{B^2}\right) > f^2 + gh_n\frac{m^2\pi^2}{B^2} = \omega_{\text{cut}}^2, \tag{40}$$

where h_n is the equivalent depth (see Hutter [16]). It is also possible to construct solutions for the longitudinal velocity component

$$U = \left\{\alpha_m \sin\left(\frac{m\pi y}{B}\right) - \beta_m \cos\left(\frac{m\pi y}{B}\right)\right\}e^{i(kx-\omega t+\pi/2)}, \tag{41}$$

where

$$\alpha_m = \phi_{km}\frac{\omega}{k}\bar{V}, \qquad \beta_m = -\frac{gh}{f}\phi_{km}\frac{m\pi}{Bf}\frac{\omega}{f}\bar{V} \tag{42}$$

and

$$\phi_{km} = \frac{k^2 + \frac{m^2\pi^2}{B^2}}{k^2 + \frac{m^2\pi^2}{B^2}\frac{\omega^2}{f^2}}. \tag{43}$$

Modifications of this type of waves in the presence of topography are called "Poincaré-type" waves by us.

REFERENCES

1. A. Arakawa and V. R. Lamb, Computational design of the basic dynamical processes of the UCLA general circulation model, *Methods Comput. Phys.* **17**, 173 (1994).
2. H. Bührer and A. H. Ambühl, Die Einleitung von gereingtem Abwasser in Seen, *Z. Hydrol.* **37**, 347 (1975).
3. V. Casulli and E. Cattani, Stability, accuracy and efficiency of a semi-implicit method for three-dimensional shallow water flow, *Comput. Math. Appli.* **27**(4), 99 (1994).
4. V. Casulli and R. T. Cheng, Semi-implicit finite difference methods for three-dimensional shallow water flow, *Int. J. Numer. Methods Fluids 15*, 629 (1992).
5. G. T. Csanady, *Circulation in the Coastal Ocean* (Reidel, Dordrecht, 1984).
6. J. K. Dukowicz and R. D. Smith, Implicit free-surface method for the Bryan–Cox–Semtner ocean model, *J. Geophys. Res.* **99**, 7991 (1994).
7. T. Gal-Chen and R. C. J. Sommerville, Numerical solution of the Navier–Stokes equations with topography, *J. Comput. Phys.* **17**, 276 (1975).
8. T. Gal-Chen and R. C. J. Sommerville, On the use of a coordinate transform for the Navier–Stokes equations, *J. Comput. Phys.* **17**, 209 (1975).
9. D. Gottlieb and S. A. Orszag, *Numerical Analysis of Spectral Methods: Theory and Applications* (Soc. Indust. Appl. Math. 1977).
10. P. Güting, *Dreidimensionale Berechnung windgetriebener Strömungen mit einem k-ϵ Modell in idealisierten Becken und im Bodensee*, Ph.D. thesis, University of Technology at Darmstadt, FB6 (1998).
11. P. Güting and K. Hutter, Modeling wind-induced circulation in the homogeneous Lake Constance using a k-ϵ-closure, *Aquatic Sci.* **60**, 266 (1998).
12. D. Haidvogel, J. Wilkin, and R. Young, A semi-spectral primitive equation ocean circulation model using vertical sigma and orthogonal curvilinear horizontal coordinates, *J. Comput. Phys.* **94**, 151 (1991).
13. K. S. Hedstrom, *User's Manual for a Semi-spectral Primitive Equation Regional Ocean-Circulation Model*, Technical Report SR-1, Institute for Naval Oceanography (July 1990).
14. C. Hirsch, *Numerical Computation of Internal and External Flows* (Wiley, New York, 1988), Vol. 1.
15. K. Hutter (Ed.), *Hydrodynamics of Lakes* (Springer-Verlag, Berlin/Vienna/New York, 1984) [CISM Lectures]
16. K. Hutter, Waves and oscillations in the ocean and in lakes, in *Continuum Mechanics in Environmental Sciences and Geophysics*, edited by K. Hutter (Springer-Verlag, Berlin/Heidelberg/New York, 1993).
17. A. Kasahara, Various vertical coordinate systems used for numerical weather prediction, *Mon. Weather Rev.* **102**, 509 (1974).
18. J. Marshall *et al.*, A finite-volume, incompressible Navier–Stokes model for studies of the ocean on parallel computers, *J. Geophys. Res.* **102** (C3), 5753 (1997).
19. J. Marshall *et al.*, Hydrostatic, quasi-hydrostatic and nonhydrostatic ocean modelling, *J. Geophys. Res.* **102** (C3), 5733 (1997).
20. N. A. Phillips, A coordinate system having some special advantages for numerical forecasting, *J. Meteorol.* **14**, 184 (1957).
21. T. J. Simons, Circulation models of lakes and inland seas, *Can. Bull. Fisheries and Aquatic Sci.* **203** (1980).
22. Y. Song and D. Haidvogel, A semi-implicit ocean circulation model using a generalized topography-following coordintate system, *J. Comput. Phys.* **115**, 228 (1994).
23. M. Taylor, J. Tribbia, and M. Iskandarani, The spectral element method for the shallow water equations on the sphere, *J. Comput. Phys.* **130** (1), 92 (1997).
24. G. Veronis, in *Numerical Models of Ocean Circulations* (Washington DC, 1975).
25. Y. Wang and K. Hutter, ADI methods applied to semi-spectral code of the shallow water equations, in preparation.
26. Y. Wang and K. Hutter, A semi-implicit semispectral primitive equation model for lake circulation and its stability performance, *J. Comput. Phys.* **139**, 209 (1998).
27. J. Wilkin and K. Hedstrom, *User's Manual for an Orthogonal Curvilinear Grid-Generation Package*, Institute for Naval Oceanography (1991).